Nanoscale

Accepted Manuscript

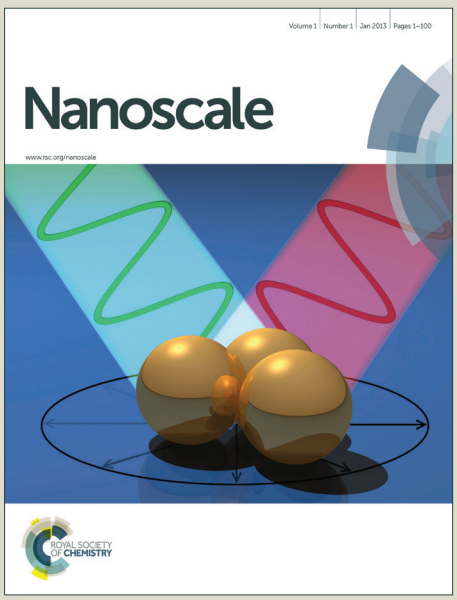

ROYAL SOCIETY OF CHEMISTRY

www.rsc.org/nanoscale

Journal Name

RSCPublishing

ARTICLE

In-situ microfluidic SERS assay for monitoring enzymatic breakdown of organophosphates

Cite this: DOI: 10.1039/xoxxoooooox

Received ooth January 2012,
Accepted ooth January 2012

DOI: 10.1039/xoxxoooooox

www.rsc.org/

Vladimir Liberman[a)], Kimberly Hamad-Schifferli, Todd A. Thorsen, Scott T. Wick, and Peter A. Carr

Corresponding author: vlad@ll.mit.edu

In this paper, we report on method to probe the breakdown of the organophosphate (OP) simulants o,s-diethyl methyl phosphonothioate (OSDMP) and demeton S by the enzyme organophosphorous hydrolase (OPH) in a microfluidic device by surface enhanced Raman spectroscopy (SERS). SERS hotspots were formed on-demand inside the microfluidic device by laser-induced aggregation of injected Ag NPs suspensions. The Ag NP clusters, covering micron-sized areas, were formed within minutes using a conventional confocal Raman laser microscope. These Ag NP clusters were used to enhance the Raman spectra of the thiol products of OP breakdown in the microfluidic device: ethanethiol (EtSH) and (ethylsulfanyl) ethane-1-thiol (2-EET). When the OPH enzyme and its substrates OSDMP and demeton S were introduced, the thiolated breakdown products were generated, resulting in changes in the SERS spectra. With the ability to analyze reaction volumes as low as 20 nL, our approach demonstrates great potential for miniaturization of SERS analytical protocols.

Nanoscale RSCPublishing

ARTICLE

Introduction

Organophosphates (OPs) are dangerous nerve agents with acute toxicities. Strategies for their disposal include degradation into less toxic species. In particular, enzymatic hydrolysis of OPs and other nerve agents by organophosphorous hydrolases (OPH)[1] and phosphotriesterases has many advantages. Biological systems are amenable to mutation to improve efficiency, which has successfully increased OPH activity by several orders of magnitude. However, assays for probing OPH activity and other degradation approaches often require handling of the nerve agents or their simulants, which are still quite toxic. Microfluidic systems are highly desirable because they can minimize the amount of reagents required in a scalable modular format.

Assays that probe breakdown products in a label-free manner are very desirable as they obviate the need to label the reaction product of interest. Raman spectroscopy is a powerful technique for label-free compound discrimination utilizing their unique vibrational signatures. However, due to inherently low Raman cross-sections, detection of neat compounds from inside a microchannel is only possible for concentrations in the range of 10-100 mM, which is not practical for monitoring enzymatic reactions. Combining Surface Enhanced Raman Spectroscopy (SERS), a label-free technique with pM detection sensitivity for small molecules, and microfluidics could yield a potentially powerful sensing platform. Thus, a method for introducing surface enhancement structures into a microfluidic channel is desired.

There are a number of studies that integrate SERS into a lab-on-chip format. Some studies inject SERS nanoparticles (NPs) directly into an analyte stream.[2-7] Mixing-post structures inside the microchannel and/or pulsed flows can address settling out nanoparticles inside the channel; however, significant signal gradients vs. measurement position along the channel still exist. To overcome such problem, liquid/liquid segmented microfluidic systems have been used successfully for nanoparticle injection.[8] In another microfluidic platform, SERS nanoparticle labels were used to measure immobilization of capture DNAs.[9]

Incorporating a pre-fabricated SERS nanostructure inside the channel has been an intriguing alternative to nanoparticle injection.[10] In some studies, silver colloid was prepared *in situ* via chemical reaction or electrodeposition.[11, 12] In other approaches, SERS silver substrates were prepared *in situ* by laser-induced photochemical synthesis from a mixture of $AgNO_3$ and sodium citrate.[13, 14] However, in all these studies, rough surfaces were produced without control of surface geometry or placement of SERS active substrates inside the channel.

Here, we introduce a novel method of photoassisted agglomeration of Ag NPs inside a microfluidic channel. In contrast to previous approaches, we assemble micron-sized clusters, which act as SERS hot spots, by controllably photo-aggregating Ag NPs at any desired location inside the channel. Our method is label-free and allows on-demand assembly of active SERS substrates directly prior to experiment to minimize potential ambient degradation of the Ag surfaces.[15] We use the Ag NP clusters to probe wild type (WT) OPH breakdown of V-agent simulants[1] o,s-diethyl methyl phosphonothioate and demeton-S (Figure 1a). Upon enzyme-mediated hydrolysis, the simulants undergo P-S bond scission to form the decomposition products, ethanethiol (EtSH) and 2-(ethylsulfanyl)ethane-1-thiol (2-EET) (Figure 1b). Direct monitoring of the evolution of the thiol-containing decomposition products probes the enzymatically-induced degradation of the simulants. The approach presented here could miniaturize and thus improve assays involving nerve agents and other highly toxic chemicals.

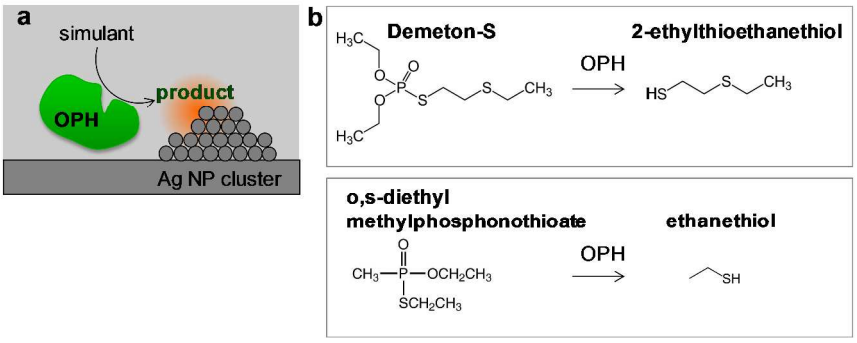

Figure 1. a. Schematic of the detection process showing simulant breakdown and trapping on the photo-assembled nanoclusters for in-situ SERS detection. b. Chemical diagram of the simulant degradation in the presence of OPH to form breakdown product. Top: demeton S degradation into 2-EET. Bottom: OSDMP degradation into EtSH.

Nanoscale

RSCPublishing

ARTICLE

Results and Discussion

Relative SERS efficiency of isolated nanoparticles

Prior to assembling NP SERS clusters, we studied relative enhancement of EtSH from isolated plasmonic nanoparticles in solution. These studies are aimed at determining the best building block for subsequent NP cluster assembly inside a microfluidic channel. Au and Ag citrate-capped NPs with sizes ranging from 30 to 100 nm were obtained in aqueous suspensions (Experimental Methods, Table 5). 100 μM EtSH was incubated with the NPs for 30 min. At this concentration, the contribution of excess EtSH in solution to the Raman signal is expected to be $<10^{-5}$. A SERS spectrum was obtained with a 785 nm excitation utilizing a portable Raman spectrometer with a fiber-probe (Experimental Methods).

For compounds of interests (Figure 1b), only limited Raman spectral data exist in the literature, primarily for EtSH;[16] thus, we acquired our own experimental Raman spectra of the neat compounds to better understand the changes arising from surface enhancement. We performed density functional theory calculations to assign spectral features between 400 and 1500 cm^{-1}. (See Experimental Methods for computational details). The spectrum of neat EtSH is dominated by the C-S stretch at 656 cm^{-1} (Figure 2a, top spectrum). A C-C stretch is observed at 1051 cm^{-1}. The other modes are combinations of a) C-S-H deformation with CH_3 rocking modes (862 and 1087 cm^{-1}) b) C-S-H deformation with CH_2/CH_3 rocking modes (738 cm^{-1}) and c) CH_2/CH_3 twist and wag modes at 1270 and 1449 cm^{-1}. Spectral assignments are summarized in Table 1.

The difference between Raman spectra of the compounds in neat form vs. on the AgNP cluster surface can be explained by the SERS surface selection rule. According to this rule, the vibrational bands that draw their intensity from the α_{zz} Raman polarizability component (z being the surface normal) undergo the strongest enhancement.[17, 18] This rule has been loosely equated with the IR spectroscopy surface selection rule, which simply states that only those bands whose transition dipole has a z component will be observed. Compared to the neat spectra, the surface-enhanced spectrum of EtSH is modified as follows (Figure 2a, bottom): the primary 656 cm^{-1} mode is downshifted by ~20 cm^{-1} and several peaks disappear (738, 862, and 1087 cm^{-1}). All the peaks that disappear involve H-S-C deformation. We thus conclude in accordance with earlier studies[16] that upon adsorption to the Ag NP, the S-H bond is broken in EtSH. The downward shift of the C-S stretch indicates strong interaction with the surface, as would be expected since the bonding occurs through the S-end of the molecule.

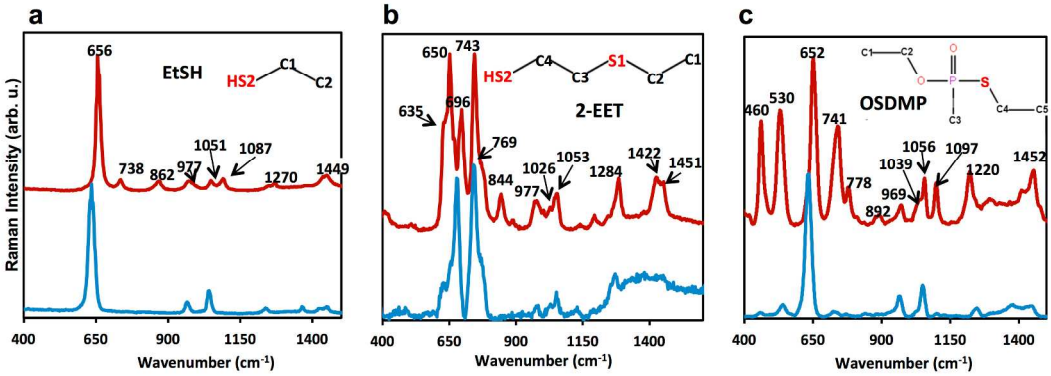

Figure 2. Raman spectra and location of major peaks for a: EtSH, b: 2-EET and c: OSDMP. In all cases, top traces show neat compound spectrum and the bottom traces show SER spectrum at saturated surface coverage on 50 nm diameter Ag NPs.

Nanoscale RSCPublishing

ARTICLE

Table 1. Vibrational Raman peak assignments for EtSH. Numeric labels on constituent atoms correspond to insets of Figure 2.

Wavenumber (cm^{-1})	Peak Assignments
656	ν(C1S)
738	δ(C1SH)+ρ_r($C1H_2$) +ρ_r($C2H_3$)
862	δ(C1SH)+ρ_{sym}($C2H_3$)
977	ν(C1C2)+ρ_r($C1H_3$)
1051	ν(C1C2)
1087	δ(C1SH)+ρ_{as}($C2H_3$)
1270	ρ_t($C1H_2$)+ρ_W($C1H_2$)
1449	ρ_t($C2H_3$)+ρ_W($C2H_3$)

Based on the above peak assignments, we determined the relative SERS enhancements by comparing the area under the C-S stretching peak in the spectrum (635 cm^{-1}) for different NP suspensions from Table 5, Experimental Methods. After normalizing peak areas to the NP surface area and taking into account relative NP concentrations, the 50 nm and 70 nm Ag NP suspensions yielded the highest signal (Table 2). The SERS signal from 50 nm Au NPs was two orders of magnitude weaker than that from Ag NPs. The difference in signal is consistent with the weaker electromagnetic enhancement predicted from Au as opposed to Ag NPs based on electromagnetic theory.[19] Therefore, for the remainder of the study, we used 50 nm Ag NPs as the SERS medium. The as-delivered 50 nm Ag NP suspension had a SPR peak at 415 nm and TEM images showed a mean diameter of 50 nm with 10% coefficient of variation (Figure 3).

For calibration of EtSH detection and determination of the detection limit in a 50 nm Ag NP suspension, we performed dilution experiments in parallel with fluorescence assays (Experimental methods). The lowest detection limit for EtSH with a 3:1 S/N ratio is 20 nM, while the corresponding detection limit for 2-EET is 200 nM. The higher detection limit for 2-EET corresponds to the lower Raman cross-section for the neat 2-EET: the relative SERS enhancement factor is comparable for both EtSH and 2-EET.

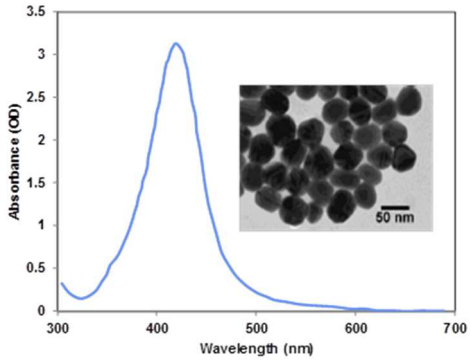

Figure 3. Absorption spectrum of the 50 nm Ag NP suspension, as delivered by the vendor. Inset shows a TEM of the NPs.

Table 2. Relative efficiency of NP suspensions in producing a SERS signal from EtSH. The numbers in the table refer to surface-area normalized Raman spectral peak at 635 cm^{-1}, corresponding to a C-S stretching mode.

Size (nm)	Ag	Au
30	0.16	
50	1	0.01
70	0.99	
100	0.15	<0.002

Nanoscale

RSCPublishing

ARTICLE

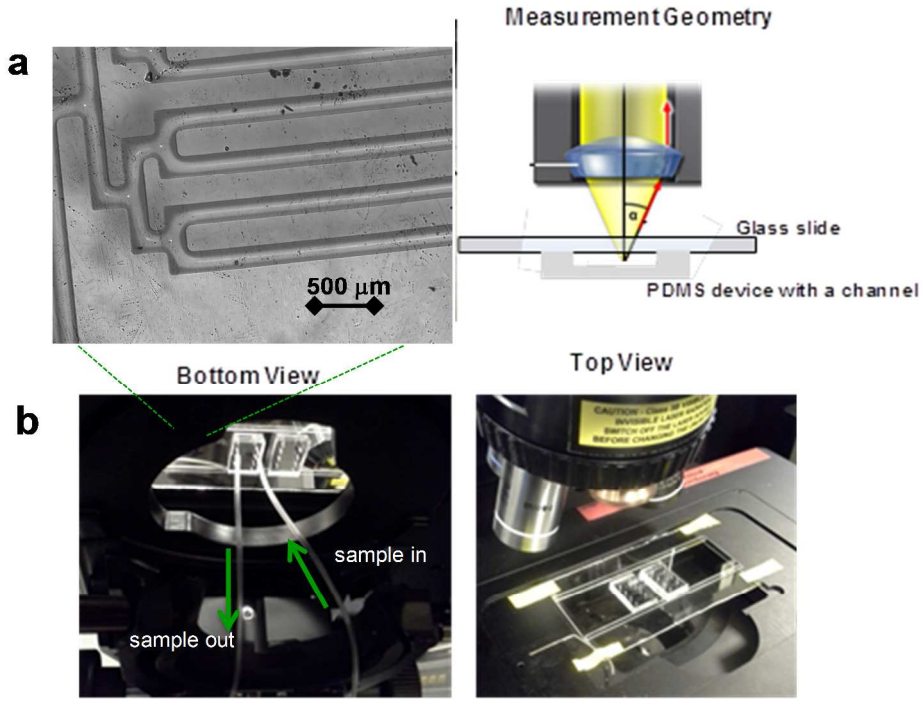

Figure 4 a. Left: Top-down micrograph of a typical PDMS microchannel device on a quartz substrate. Right: schematic of the light path through the microscope objective and into the microfluidic device. b. Setup for SERS cluster formation and subsequent Raman measurement, utilizing a commercial confocal Raman microscope. Left: view from the bottom, showing the PDMS side of the chip. Right: View from the top of the chip affixed to the microscope scanning stage.

Formation of SERS active clusters in microfluidic channels

Deposition of fresh clusters

We demonstrated formation of SERS active clusters on demand inside the microchannel from a NP solution. As-supplied, 50 nm Ag NP suspension was concentrated by 50X by centrifugation and injected into the microchannel device (Figure 4a,b) at flow rates of 5-10 µl/min. After ≤30 min of flow, spontaneous NP precipitation was observed, mainly near the microchannel exit and entrance. This seeded area was then laser-irradiated at 532 nm, 50 mW through the 40X objective (corresponding to ~1 MW/cm^2 at the sample surface). Within 1-2 min of irradiation, bright spots appeared inside the microchannel, as monitored on the viewing camera attached to the Raman microscope. Slow rastering of the focused beam, using the motorized XY stage attached to the Raman microscope allowed us to grow the size of these bright Ag clusters to tens of µms (Figure 5a). Once clusters were formed in the microchannel, they remained intact for hours with no signs of being displaced by liquid flow.

In the post-experimental inspection of the microfluidic device, we found that while spontaneous NP deposition occurred on both the PDMS and the glass slide, the laser-induced aggregates were exclusively present on the glass substrate inside the channel. SEM imaging of the glass substrate (Figure 5b) showed aggregates of individual Ag NPs, but no evidence of fusing or melting.

Once the bright clusters were formed inside the channel, the Raman microscope was switched into the measurement mode and the clusters were interrogated. Initially, both 785-nm excitation (to correlate with solution measurements of the previous section) and 532-nm excitation were used. The 532-nm excitation, however, was found to increase the signal strength by more than an order of magnitude over that of 785-nm excitation, while preserving spectral features. This enhancement of the signal is partially explained by the $1/\lambda^4$ dependence of Raman cross-section on excitation wavelength and by better overlap of 532-nm excitation with plasmonic resonance of Ag clusters. Thus, for the experiments described here, 532-nm excitation was used.

For acquisition of SERS spectra, the 532 nm excitation laser was attenuated by 10x from the intensity used for cluster formation. With only 1-2 sec of acquisition time, we observed

an extremely intense spectrum from within the cluster, and a considerably weaker spectrum just outside the bright cluster in the area of precipitated NPs (Figure 5c, upper two traces). By contrast, no Raman signal was observed from outside of the areas containing precipitated NPs. Spectral reproducibility of the citrate signal was verified by measuring SERS spectra at multiple cluster locations. (See Supplemental Information, Figure S1).

The as-supplied Ag NPs are electrostatically stabilized by surfaced citrate groups (Experimental Methods). Thus, in a control experiment, we obtained a Raman spectrum of aqueous 0.1 M sodium citrate (Figure 5c, bottom). This spectrum shows three major peaks: 1413, 953 and 842 cm^{-1}. The 1650 cm^{-1} feature arises from the water background[20] and can be ignored. These peaks are consistent with a previously observed Raman spectrum of sodium citrate and have been assigned to the COO stretch, C-COO stretch and CCCC-O stretch, respectively.[20] For this control experiment, the solution concentration of sodium citrate is several orders of magnitude higher than what is present in the precipitated Ag NPs in the channel. Therefore, we expect to see no contribution from the solution spectrum when interrogating the precipitated NPs; instead, the Raman spectra from the precipitated Ag cluster (upper two spectra in Figure 5c) must be attributed to surface-enhanced form of citrate capping. These SERS spectra differ markedly from the solution spectrum. The 1413 cm^{-1} feature, present in the solution spectrum, is blue-shifted to 1361 cm^{-1} inside the cluster (Figure 5c, upper trace). Additionally, new features arise at 1582 and 1608 cm^{-1}, which are weak outside the cluster, but are increased for the spectrum from within the cluster. Furthermore, a new feature is seen at ~1140 cm^{-1} in the area outside the cluster, which blueshifts strongly to the 1073 cm^{-1} feature inside the cluster. To aid in interpretation of these spectral features, we refer to an earlier SERS study of citrate interaction with Ag colloids.[20] That study reported that upon boiling of the aqueous colloid suspension, the surface adsorbed citrate underwent decomposition into acetonedicarboxylic acid.[20] This decomposition produced intense Raman peaks between 1550 to 1600 cm^{-1} region, at 1388 and 1100 cm^{-1}, consistent with the spectral features observed by us on aggregated NP clusters (Figure **5**c). We, therefore, suggest that laser-induced agglomeration of Ag NPs leads to partial decomposition of surface citrate species, potentially due to laser-induced heating.

Mechanism of Photoinduced Cluster Formation

Because the intensity of the focused 532 nm laser beam inside the microchannel can reach ~1 MW/cm^2, laser-induced heating of NPs in solution should be considered. Previous calculations and experimental measurements have considered heating of plasmonic NPs on glass substrates in aqueous media for 100 nm Au NPs irradiated at 488 nm.[21] Using Mie scattering theory to scale the absorption cross-section for our Ag NPs at 532 nm, we predict that laser heating of isolated NPs is negligible for our conditions (<5°C). Once the NPs are agglomerated, higher laser absorbance from the cluster might be expected, thus producing higher temperature rises. Indeed, these elevated surface temperatures are consistent with the modified surface citrate spectra from precipitated and aggregated NPs. However, no bubble formation was observed at any point during cluster photoassembly. Thus, even allowing for superheating of aqueous suspension, the absence of bubbles suggests that our nanocluster surface temperatures do not exceed 200 °C.[22]

In the absence of laser-induced melting of NPs, a likely mechanism for agglomeration is laser-induced desorption of surface citrate species that nominally stabilize the NPs in solution. Decomposition of citrate groups (Figure 5c) would lead to colloidal precipitation out of solution. Additionally, at incident laser intensities exceeding 1 MW/cm^2, long range optical forces between plasmonic NPs can overcome repulsive colloidal electrostatic forces and cause the particles to permanently assemble.[23]

Photoaggregation of pre-functionalized Ag NPs

Having photo-aggregated citrate-capped NPs, we next investigated aggregation of Ag NPs that had been previously thiolated. 2 μM of 2-EET was added to the Ag NP suspension prior to injection into the microchannel. The reason for using 2-EET in these experiments is because of its higher boiling point (180 °C) over that of EtSH (35 °C). Thus, decomposition of 2-EET during laser-induced cluster assembly due to surface temperature rise is less likely than that of EtSH.

The Raman spectra of 2-EET has not been previously reported in the literature. We obtained separately a Raman spectrum of neat 2-EET and its SERS spectrum utilizing a 50 nm Ag NP suspension at a surface saturation concentration of 10 μM. Spectral assignments (Table 3) were performed utilizing density functional theory calculations (Experimental Methods). The neat spectrum of 2-EET (Figure 2b, upper trace) has multiple peaks in the C-S stretch region (650-750 cm^{-1}) due to the presence of two sulfur atoms. The 844 and 977 cm^{-1} peaks involve deformation modes of the sulfur atom at the end of the chain, whereas the 1053 cm^{-1} peak involves the vibrational modes of the sulfur atom in the middle of the carbon chain. In the surface enhanced spectrum (Figure 2b, lower trace), the 696, 844 and the 977 cm^{-1} peaks are greatly diminished. All these peaks involve H-S-C deformation of the end sulfur atom and the 696 cm^{-1} peak additionally involves the S-C stretch of the sulfur in the middle of the chain. We propose that the 2-EET molecule adsorbs through de-protonation of the end sulfur atom. Thus, the reduction of the 696 cm^{-1} peak intensity is caused by both cleavage of the S-H bond and the lower surface enhancement of the S-C stretch for the carbon atom in the middle of the chain.

Once the NPs pre-treated with 2-EET were photoaggregated inside the channel, we performed a spatial Raman mapping scan of the resulting Ag cluster. To capture the relevant C-S stretches while reducing the overall spectral mapping time, we restricted the spectral scan region to 450–950 cm^{-1}. A typical spectrum from the bright area of the Ag cluster revealed three prominent peaks between 630 and 800 cm^{-1} (Figure 5d, middle trace). Integrating the signal over this spectral region at every spatial point of the Raman map ('+' symbols in Figure 5e), we obtain the spatial distribution of peak intensities (Figure 5f). Spectra corresponding to the dark areas of this Raman map (Figure 5d, bottom trace) are readily matched to bulk PDMS spectra from separate experiments. Since the microfluidic device is interrogated through the glass substrate with the confocal Raman microscope, the bulk PDMS Raman signal is expectedly smaller than the SERS 2-EET signature.

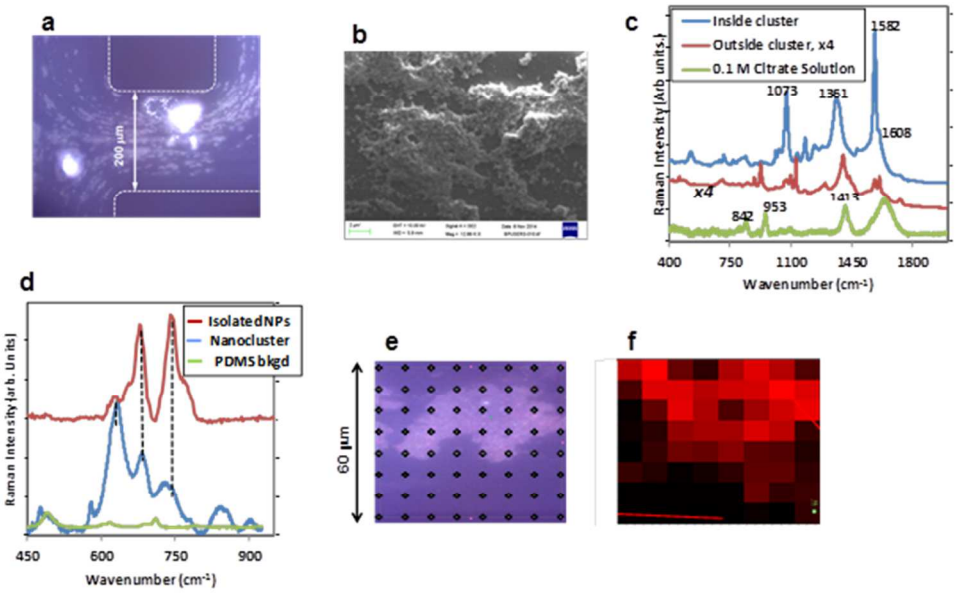

Figure 5 a. Photoaggregated Ag clusters formed inside the microchannel. b. SEM of laser-agglomerated Ag cluster inside the microchannel. c. Top trace: Raman spectrum from the bright cluster of a. Middle trace: Raman spectrum, multiplied by a factor of 4, from the area with precipitated Ag NPs outside the cluster. Bottom trace: reference Raman spectrum of 0.1 M sodium citrate solution. d. Top trace: reference SERS spectrum of 2-EET from a 50 nm Ag NP aqueous suspension. Middle trace: SERS spectrum of a photo-aggregated NPs that had been pre-treated with 2-EET from e . Bottom trace: Raman spectrum from the PDMS microchannel outside the nanocluster. e. Spatial Raman mapping of a thiolated Ag nanocluster formed in-situ after laser irradiation--a micrograph of the nanocluster showing Raman measurement location with + symbols. f. Integrated intensity of the C-S stretch peak corresponding to the locations marked with + symbols in e.

The spectrum corresponding to the bright spots in Figure 5f can be compared to the surface enhanced spectrum of the 2-EET from isolated Ag NPs (middle vs. top trace of Figure 5d). The three peaks at 633, 680 and 785 cm^{-1} (dashed lines) correspond to C-S stretches and CH_2 rocking modes (Table 3 and Figure 2b). The weaker 850 cm^{-1} peak of the thiolated cluster (Figure 5d, middle trace) may correspond to the 2-EET neat feature (Figure 2b, top trace). The full spectral set, corresponding to Figure **5**f, shown in Supplemental Information Figure S2, shows excellent spectral reproducibility of the peaks.

The reason for the difference between relative peak intensities of the control 2-EET spectra and thiolated nanocluster spectra may be twofold. First, the species trapped inside the nanocluster could have a different binding geometry to the Ag surface, which would influence the surface enhancement factor.[17] Second, the spectrum from the cluster could be different than the surface enhanced spectrum for the 2-EET due to surface heating of the nanocluster during photoassembly.

The results presented above suggest that photoaggregation of pre-treated NPs provides significant signal enhancement over isolated NPs. We can, for instance, envision trapping reaction products onto NPs in a separate microfluidic chamber, and then photoaggregating the NPs for sensitive SERS detection, in similarity to previous studies that induced NP dimerization for higher SERS intensity of the adsorbates.[24]

Table 3. Vibrational peak assignments for 2-EET from quantum chemical calculations. Numeric labels on constituent atoms correspond to insets of Figure 2.

Wavenumber (cm^{-1})	Peak assignments
635	ν(C4-S2) + ν(C2-S1)
650	ν_{as}(C2-S1-C3) + ν(C4-S2)
696	δ(H-S2-C4) + $\rho_r(C4H_2)$+$\rho_r(C3H_2)$+ν(C3-S1)
743	δ(S1-C3-C4) + ν(C4-S2)
769	$\rho_r(C2H_2)$+$\rho_r(C1H_2)$
844	δ(H-S2-C4) + $\rho_t(C4H_2)$ + $\rho_r(C3H_2)$
977	δ(H-S2-C4) + $\rho_r(C4H_2)$ + $\rho_t(C3H_2)$
1026	ν(C3-C4) + ν(C1-C2)
1053	δ(C2-S1-C3) + ν(C3-C4) + ν(C1-C2)
1284	$\rho_t(C3H_2)$ + $\rho_t(C4H_2)$
1422 -1451	$\rho_w(C2H_2)$, $\rho_w(C3H_2)$, $\rho_w(C4H_2)$

SERS spectra of simulants and degradation products inside the microchannel

OSDMP+ enzyme

Having formed the photoaggregated cluster from citrate-capped NPs as described above (Figure 5a), we then used such clusters to monitor enzymatically-induced simulant decomposition. OPH hydrolyzes OSDMP to form EtSH, (Figure 1b) which can be detected by SERS once the molecule is trapped on the Ag NP cluster. 9 μM OPH enzyme and 100 μM OSDMP in water were mixed offline and then immediately injected into the microchannel (Figure 6a). Raman spectra from the aggregated Ag nanoclusters were acquired at 0, 2, 8, 13 and 30 min after injection (Figure 6b). For each spectrum, a fresh surface of the cluster was used by translating the Raman excitation beam by 2 μm. An attenuated laser beam at 5 mW incident power was used with 2 s acquisition times. As a control experiment, we formed a fresh cluster in a parallel microchannel, injected 100 μM OSDMP without the OPH enzyme and monitored surface enhanced Raman spectrum inside the channel analogously (Figure 6c).

Analyzing the time-dependent evolution of spectra in Figure 6b, we observe only an original citrate layer at time 0 min with spectral features between 750 and 850 cm^{-1}. At longer times, a peak at 630 cm^{-1} increases with time whereas the citrate-related features diminish. The 630 cm^{-1} peak is attributed to the C-S stretch of EtSH, as it evidently displaces the surface citrate species. The integrated C-S peak intensity (inset, Figure 6b) exhibits a slow rise as a function of time up to 8 min, followed by a rapid jump in signal and eventual saturation at 30 min. The shape of the curve does not follow simple Langmuir adsorption kinetics[25] or the enzyme decomposition kinetics as measured separately by a fluorescence assay. Rather, the double saturation of the curve may be indicative of multiple adsorption sites on the surface and is reminiscent of multiple saturation loadings, observed for liquid adsorption onto zeolites.[26] Another possibility is that the early saturation of signal refers to adsorption of neat OSDMP (see also Figure 6c and discussion below), whereas the strong signal increase corresponds to adsorption of EtSH, formed by the enzyme dissociation reaction.

The control experiments with pure OSDMP in the absence of enzyme (Figure 6c) also show a surface enhanced Raman peak, but it is 3 times weaker than when the enzyme is present (top vs. bottom trace in the figure).

To understand the results of these experiments, we performed vibrational peak assignments of neat OSDMP and its surface enhanced spectrum utilizing 50 nm Ag NP suspension with a surface saturation concentration of OSDMP (100 μM). For the neat OSDMP, we have performed density functional theory calculations to assign the Raman peaks. The spectrum of neat OSDMP (Figure 2c, top) contains several strong peaks in the region below 800 cm^{-1}. The 652 cm^{-1} peak is associated with the C-S stretch. The 460 cm^{-1} is a combination of P-S stretch and PO-C deformation. The 530 cm^{-1} peak is the P-S stretch and the 741 cm^{-1} feature is the P-O stretch. The 1220 cm^{-1} peak is the P=O stretch. The other peaks are associated with the carbon-chain backbone. Peak assignments from density functional theory calculations are summarized in Table 4.

Substantial changes are observed in the surface enhanced spectrum compared to that of the neat compound. The major peaks of the surface enhanced spectrum (Figure 2c, bottom) greatly resemble the spectrum of adsorbed EtSH (Figure 2a, bottom): the largest peak is the downshifted C-S stretch. Other peaks correspond to the C-C stretch for the carbons attached to sulfur. Notably, the ratio of the P-S stretch to the C-S stretch is reduced from 1:1.6 for the neat compound to 1:16 for the surface enhanced spectrum. The P=O and the P-O stretches are reduced by a similar amount. Based on previous studies of OSDMP hydrolysis,[27] spontaneous decomposition of OSDMP occurs over many hours and is unlikely on the timescale of our Raman measurements. Therefore, we postulate that the similarity between OSDMP and EtSH surface enhancement spectra is due to dissociative adsorption of OSDMP on Ag surface via P-S bond cleavage. Uniform reduction of all the vibrational frequencies associated with the phosphono group, regardless of their bond orientation further suggests that OSDMP molecule is partially decomposed upon adsorption.

In view of the above peak assignments, we can now interpret the Raman signal at 630 cm^{-1} observed from the Ag cluster after injecting the control OSDMP compound into the microchannel (Figure 6c, top). This signal is due to partial dissociation of the OSMDP upon surface adsorption. Close examination of the control spectrum reveals the presence of small features at 538 and 726 cm^{-1} not present in the OSDMP + enzyme spectrum (Figure 6c, bottom). These additional spectral features appear in the surface enhanced spectrum of OSDMP (Figure 2c, bottom), but not in that of EtSH (Figure 2a, bottom). These results suggest that enzymatic activity breaks down OSDMP to products that differ from OSDMP spontaneously adsorbed onto Ag NPs.

Table 4. Vibrational peak assignments for OSDMP from quantum chemical calculations. Numeric labels on constituent atoms correspond to insets of Figure 2.

Wavenumber (cm^{-1})	Peak Assignments
460	δ(POC2)+ν(PS)
530	ν(PS)
652	ν(C4S)
741	ν(P-O)
778	ν(P-C3)
892	ν(C1-C2)
969	ν(C4-C5)
1039	ν(C2-O)+$\rho_t(C2H_2)$+$\rho_r(C1H_3)$
1056	ν(C4-C5)+$\rho_r(C5H_3)$
1097	$\rho_r(C1H_3)$
1220	ν(P=O)
1452	$\rho(C5H_3)$

Demeton S + Enzyme

We then investigated OPH-induced decomposition of the simulant demeton S, which is hydrolyzed into 2-EET (Figure 1b). 3 μM WT OPH was mixed with 100 μM demeton S and

injected into a microchannel with a freshly agglomerated Ag cluster. Raman data were collected as a function of time in a similar fashion as above. The surface enhanced Raman spectra (Figure 6d) at short times are dominated by pre-existing surface citrate species, with major peaks between 750 and 950 cm^{-1}. However, at longer times, these spectral peaks diminish in intensity and, instead, three thiol-related features emerge between 650 and 750 cm^{-1} (dashed lines). These features can be related to the 2-EET spectrum (Figure 2b and Figure 5d). The growth of these features represents clear evidence that the photoaggregated cluster is trapping species injected into the microchannel. These results suggest that the OPH enzyme is active in the microfluidic channel, and that its activity results in a measurable change in the SERS spectrum. The lower signal–to-noise of the spectra is consistent with the lower Raman cross-section of neat 2-EET as compared to the neat EtSH. Because of the low signal-to-noise, we are not able to properly perform detailed spectral assignments of these peaks, which will be the subject of future studies.

Fluorescence studies of OPH activity

We confirmed OPH activity for both demeton S and OSDMP by a bulk fluorescent thiol assay (Life Technologies, Measure-IT Thiol Assay). Fluorescence increased with time (Figure 7, solid lines), indicating production of a free thiol in the presence of the OPH and thus, confirming breakdown of the OSDMP into EtSH (Figure 7a) and demeton S into 2-EET (Figure 7b). Fluorescence did not increase for the reagents with no OPH present (dashed lines, Figure 7 a,b), suggesting breakdown was specific to the presence of the OPH activity.

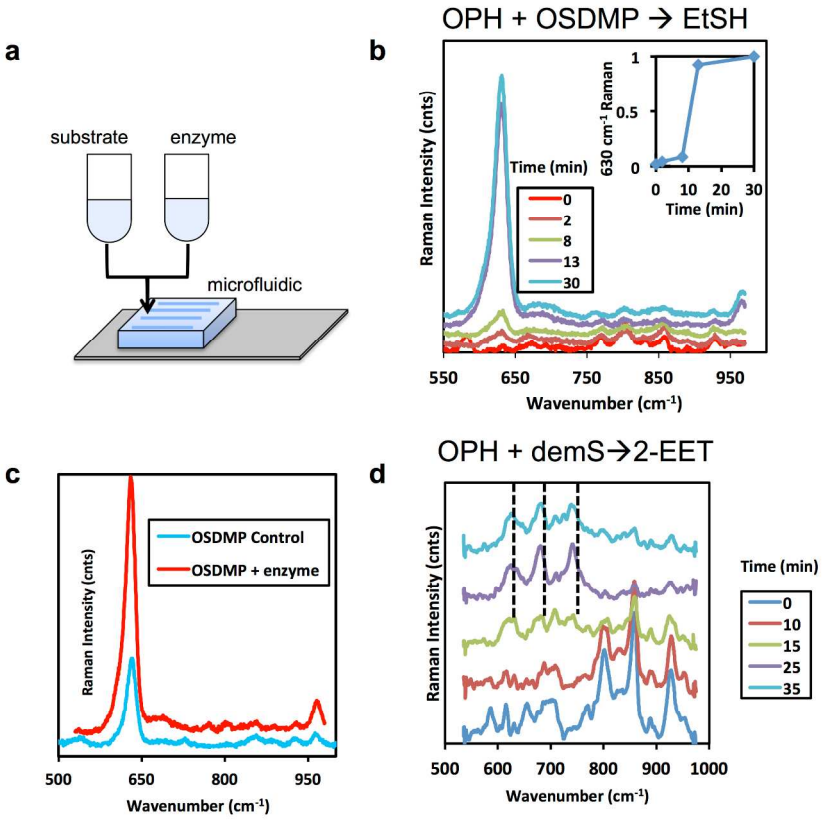

Figure 6a. Schematic of the experimental procedure involving mixing OPH with substrate simulant offchip and injecting the mixture into a microfluidic device. b. Time evolution of surface-enhanced Raman spectra from a Ag cluster inside the microchannel after a mixture of OSDMP and OPH enzyme have been injected into the microfluidic device. The inset shows integrated 630-cm^{-1} peak intensity vs. time. c. Top trace: surface-enhanced Raman spectra from a Ag cluster after OSDMP and OPH enzyme injection after 30 min. Bottom trace: surface-enhanced Raman spectra from a Ag cluster after OSDMP control injection after 30 min. d. Time evolution of surface-enhanced Raman spectra from a Ag cluster inside the microchannel after a mixture of demeton S and OPH enzyme have been injected into the microfluidic device. Dashed lines show location of three peaks attributable to thiol-related vibrations.

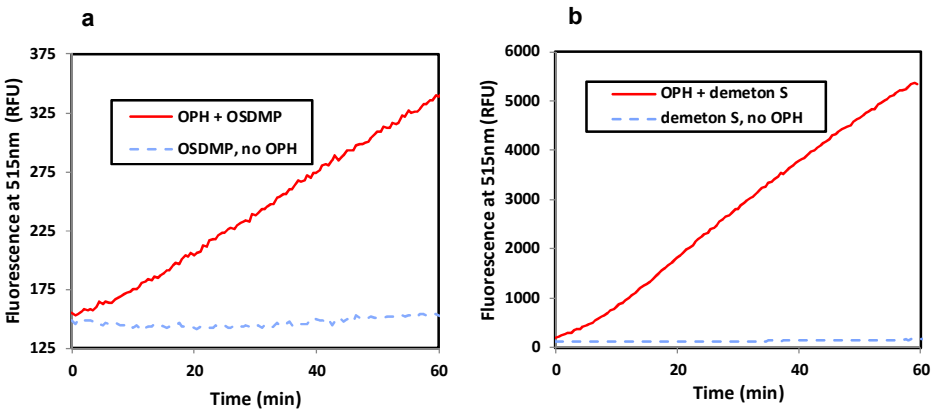

Figure 7. Monitoring simulant degradation with a fluorescent assay. a. Solid trace: OSDMP breakdown fluorescence signature in the presence of OPH. Dashed trace: control experiment with no OPH. b. Solid trace: demeton S breakdown fluorescence signature in the presence of OPH. Dashed trace: control experiment with no OPH.

Summary

We have been able to form SERS active clusters inside a microfluidic device using photo-assisted aggregation and use these to measure the activity of OPH on the OSDMP and demeton S substrates. The active SERS clusters are formed on demand prior to analysis, eliminating concerns of surface degradation with time. The microfluidic channel volume is approximately 20 nl, and assays used only 0.5 ng of demeton S or 0.3 ng OSDMP, and only 2-6 ng of the OPH enzyme, demonstrating the potential to miniaturize an assay that requires highly toxic reagents. "Soft assembly" of SERS clusters was demonstrated from Ag NP building blocks with no visual evidence of NP fusing or decomposition. We have also demonstrated the possibility of functionalizing Ag NPs in a separate chamber and then controllably photo-aggregating these particles inside a microfluidic channel for much greater SERS sensitivity than would be achieved by attempting to interrogate isolated NPs. Because SERS is a label-free technique, this approach has the potential to probe a broad range of enzymatic assays with high specificity.

Experimental Methods

Materials and instrumentation

Ethanethiol (EtSH, 97%) was purchased from Sigma Aldrich. 2-(ethylsulfanyl)ethane-1-thiol (2-EET) was ordered from American Custom Chemicals. demeton-S was purchased from Chem Service, Inc., (CAS # 126-75-0). OSDMP (o,s-diethyl methyl phosphonothioate, CAS# 2511-10-6) was purchased from Alfa Aesar. Sodium citrate tribasic dihydrate (≥99.5%) was purchased from Sigma Aldrich. All the above chemicals were used without further purification either in the neat form, or diluted, as specified.

All the Ag and Au NP suspensions used in the study were ordered from Nanocomposix, Inc with a citrate termination. Table 5 summarizes particle diameters and aqueous concentrations. A citrate capping group is ideal for SERS studies because it is easily displaceable with other molecules, but offers a high degree of electrostatic stabilization for NPs in suspensions. For most SERS experiments, 50 nm Ag NP aqueous suspension was used at a concentration of 0.02 mg/cc, which corresponded to $4x10^{10}$ particles/cc.

Enzyme synthesis

50 ml of TB + 100 μg/ml ampicillin + either 1 mM $CoCl_2$ or 100 μM $ZnCl_2$ was inoculated with a colony of DH5a containing the plasmid pUC19.+ OPH-wt and grown overnight at 30 °C. A 5 ml aliquot was used to inoculate each of 2x 1L of TB + 100 μg/ml ampicillin + either 1mM $CoCl_2$ or 100 μM $ZnCl_2$. The production cultures were grown at 180 rpm for 42 hours at 30 °C to allow OPH to constitutively express. Bacteria were harvested at 5000 rpm for 20 min. Bacterial pellets were re-suspended in 20ml of pellet wash buffer and transferred to a 50 ml conical tube. The pellet wash buffer consisted of 10 mM KPO_4 + 10 mM KCO_3 + either 50 μM $CoCl_2$ or 10 μM $ZnCl_2$ pH 6.7. Bacteria were re-pelleted at 5000 rpm, 20 min.

Table 5. Size, material and concentration of the aqueous suspension of plasmonic NPs pre-screened for this study.

Size (nm)	Material	Concentration (#/cc)
30	Ag	$1.5x10^{11}$
50	Ag, Au	$4x10^{10}$
70	Ag	$1.2x10^{10}$
100	Ag, Au	$3.5x10^{9}$

Pellets were re-suspended in 4 volumes (pellet w/v) of ice cold KCO_3 lysis buffer and sonicated 4 x 1 minute on ice at 70% amplitude setting, with 1 minute incubation on ice in between each sonication. The KCO_3 lysis buffer consisted of 10 mM KCO_3 + either 50 μM $CoCl_2$ or 10 μM $ZnCl_2$ pH 6.7. Insoluble material was pelleted at 50,000xg for 30 min at 4 °C and discarded.

To the aqueous soluble lysate, a 1/5th volume of KCO_3 buffer + 2.4% protamine sulfate solution was added dropwise over the course of 5 min while mixing on an ice bath. The solution was allowed to continue mixing an additional 10 min once the

addition of protamine sulfate was completed. The precipitate was pelleted at 50,000xg for 20 min at 4 C and discarded.

To the aqueous soluble lysate, 25.8 g of ammonium sulfate was added per 100 ml of lysate over the course of 30 min to create a 44% saturated solution. The solution was allowed to continue mixing on an ice bath an additional 1 h once the addition of ammonium sulfate was completed. The precipitate was pelleted at 50,000xg for 1 h at 4 °C.

The supernatant was discarded and the pellet was re-suspended in 20ml KPO4 pH 6.7 buffer (10mM KPO_4 + either 50 μM $CoCl_2$ or 10 μM $ZnCl_2$). The re-suspended pellets were dialyzed against 2L KPO_4 pH6.7 buffer for 4 hours at 4 C, then against a second 2 L KPO_4 pH 6.7 buffer overnight at 4 °C.

Any precipitate remaining after dialysis was pelleted at 50,000xg for 20 min at 4 °C and discarded. The aqueous solution was loaded onto an SP-Sepharose column pre-equilibrated with KPO_4 buffer pH 6.7 at 0.5ml/min in order to bind OPH to column matrix. Protein was eluted with a 0-200 mM KCl salt gradient in KPO_4 pH6.7 buffer. Fractions were analyzed by SDS-PAGE to determine fractions containing OPH. Fractions were pooled then dialyzed against 2 L KPO_4 pH 8.3 buffer for 4 hours at 4 °C, then against a second 2 L KPO_4 pH 8.3 buffer overnight at 4 °C.

Any precipitate remaining after dialysis was pelleted at 50,000xg for 20 min at 4 °C and discarded. The aqueous solution was loaded onto a DEAE column pre-equilibrated with KPO4 buffer pH 8.3 (10 mM KPO_4 + either 50 μM $CoCl_2$ or 10 μM $ZnCl_2$) at 0.5 ml/min and the flow through collected as OPH does not bind DEAE under these conditions. Fractions were analyzed by SDS-PAGE to confirm fractions containing OPH. Fractions were pooled then concentrated using Amicon-15 centrifugal concentrators (10,000MWCO) (Millipore, Inc) until A280 was greater than 1.6 (corresponding to OPH concentration >2 mg/ml ; co-extinction coefficient 58,000). Final solution was brought to 50% glycerol (by weight) and stored at -20 °C.

Computational details

The quantum chemical density functional theory (DFT) calculations were performed with a Jaguar software package (Schrodinger Corporation).[28] All calculations were performed for isolated molecules with no solvent effects. Quantum mechanical ground-state geometry optimizations were performed using a gradient-corrected Perdew-Burke-Ernzerhof local and nonlocal exchange and correlation functional (PBE)[29] and the 6-31G** basis set.[30] Once the lowest energy conformers were identified, single point energy calculations with the same functional and basis sets as above were performed to compute vibrational frequencies and Raman intensities. Computed vibrational frequencies were matched with experimental data over the range of 500 to 1500 cm^{-1}.

Microfluidic device fabrication

Microfluidic Device Mold Fabrication

The mold fabrication process was based on previously reported soft lithography methods.[31] The mold for the microchannel pattern were prepared by patterning two layers of ~15 μm thick positive AZ9260 photoresist (AZ Electronic Materials) on a 3" silicon wafer followed by a soft bake at 90 °C. The microchannel design, reproduced as a high resolution transparency mask (-20,000 dpi, CAD Art Services, Brandon, OR), was used to pattern the wafers using a contact aligner (800 mJ exposure). After developing in patterned wafer, the mold was silanized with vapor phase trimethylchlorosilane (Sigma Aldrich, Saint Louis, MO) for ~2 min to facilitate PDMS mold release in the subsequent device fabrication protocol.

PDMS Microfluidic Device Fabrication and Packaging

The microchannels were subsequently fabricated from the mold in poly(dimethylsiloxane) (PDMS) silicone rubber (Sylgard 184, Dow Corning, Midland, MI). Sylgard 184 is a two-part thermal cure silicone rubber (Parts A and B). To prepare the silicone, 10:1 Parts A:B was mixed and degassed, and poured onto the resist-patterned mold to a thickness of ~4mm. The PDMS coated mold was subsequently cured in a convection oven for 25 min at 75 °C.

After the thermal cure, a blunt-tipped 20G surgical steel Luer stub was used to punch the inlet and outlet holes at the end of the microchannels. After punching, an isopropyl alcohol wash was applied to remove debris followed by drying under a nitrogen stream. The processed PDMS microfluidic device then bonded to a 0.5 mm thick quartz slide (SPI Supplies, Chester, PA) channel-side down by first activating the slide and PDMS surfaces with air plasma followed by passive hermetic sealing of the microchannel-patterned side of the PDMS part to the quartz slide. The plasma creates hydroxyl groups on both the PDMS and quartz surfaces, initiating a condensation reaction and covalent bond formation when the surfaces are brought together. To strengthen the bond between the PDMS part and slide, the composite device was post-baked in the convection oven for 24 h at 75°C prior to use.

A micrograph of a typical microfluidic device used for SERS reaction testing is shown in Figure 4a. The interior depth of the channels is 30 μm and the width of the channel is 150 μm. The length of the channels between inlet and outlet is 5 mm.

Thiol quantification by Fluorescent assay

Thiol quantification was performed in solution by fluorescent assay kits purchased from Life Technologies (Measure-iT™ Thiol Assay Kit) or by Arbor Assays DetectX Protein Thiol Fluorescent Detection Kit. Ethanethiol was incubated with the Measure-iT thiol quantitation reagent at a 1:100 dilution in water for at least 15 min at room temperature.

For DetectX, the assay reagent (ThioStar Thiol Detection Reagent) was dissolved in DMSO prior to use and used at a 5-fold dilution in the kit assay buffer. Fluorescence ($\lambda_{excitation}$ = 495 nm, $\lambda_{emission}$ = 515 nm for Measure-iT, Life Technologies; $\lambda_{excitation}$ = 400 nm, $\lambda_{emission}$ = 504 nm for DetectX, Arbor Assays) was measured on a fluorescent plate reader (Molecular Devices SpectraMax M5) in a black 96-well plate at room temperature. Reaction volumes were 100 μL, and reagents were used as freshly prepared whenever possible.

Raman Instrumentation

Solution-based measurements were performed using a fiber-probe based spectrometer (Avantes, AvaRaman 785) with a 785 nm excitation at 300 mW power. The spot size at the focus of the probe inside the solution was 320 μm. The samples, containing either neat compounds in liquid phase, or NP suspensions were placed in a Shorty 2 mL vial (Sigma Aldrich). The Raman spectra were acquired by positioning the vial within

the working distance of the focusing probe (1 cm from probe tip) and measuring the spectrum through the glass vial walls.

Raman measurements inside a microfluidic channel were performed using a confocal Raman microscope (LabRam HR). For that work, 785 nm, 50 mW and 532 nm, 5 mW excitation wavelengths were used through a 40x long working distance objective with 0.55 NA. To obtain SERS spectra, typical acquisition times were 2 s.

To accommodate the microfluidic device on the microscope stage, the center section of the stage was removed and the microfluidic device was attached face down so that the quartz slide faced the microscope objective. In this fashion, the incident laser light from the microscope was incident on the microfluidic channel through the quartz side, avoiding potentially strong Raman signal of the PDMS. The inlet and outlet Tygon tubes were attached from underneath the microscope stage with the Luer stub fitting (Figure 4b).

Acknowledgements

This work was sponsored by the Defense Advanced Research Projects Agency under Air Force Contract FA8702-13-C-0007. The views, opinions, and/or findings contained in this article/presentation are those of the author(s)/presenter(s) and should not be interpreted as representing the official views or policies of the Department of Defense or the U.S. Government.

V.L. would like to thank Dr. S. Kwak of Schrodinger Corporation for useful discussions.

References

1. A. N. Bigley, C. Xu, T. J. Henderson, S. P. Harvey and F. M. Raushel, *Journal of the American Chemical Society*, 2013, **135**, 10426-10432.
2. S. Pahlow, A. Marz, B. Seise, K. Hartmann, I. Freitag, E. Kammer, R. Bohme, V. Deckert, K. Weber, D. Cialla and J. Popp, *Engineering in Life Sciences*, 2012, **12**, 131-143.
3. G. L. Liu and L. P. Lee, *Applied Physics Letters*, 2005, **87**, 74101-74101.
4. S. Lee, J. Choi, L. Chen, B. Park, J. B. Kyong, G. H. Seong, J. Choo, Y. Lee, K.-H. Shin, E. K. Lee, S.-W. Joo and K.-H. Lee, *Analytica Chimica Acta*, 2007, **590**, 139-144.
5. Q. Ly Xuan, L. Chaesung, S. Gi Hun, C. Jaebum, D. Ki Jun and Y. Seoung-Kyo, *Lab on a Chip*, 2008, **8**, 2214-2219.
6. X. Lu, D. R. Samuelson, Y. Xu, H. Zhang, S. Wang, B. A. Rasco, J. Xu and M. E. Konkel, *Analytical Chemistry*, 2013, **85**, 2320-2327.
7. N. Visaveliya, S. Lenke and J. M. Koehler, *ACS Applied Materials & Interfaces*, 2015.
8. K. R. Strehle, D. Cialla, P. Rosch, T. Henkel, M. Kohler and J. Popp, *Analytical Chemistry*, 2007, **79**, 1542-1547.
9. K. K. Strelau, R. Kretschmer, R. Moller, W. Fritzsche and J. Popp, *Analytical and Bioanalytical Chemistry*, 2010, **396**, 1381-1384.
10. R. M. Connatser, M. Cochran, R. J. Harrison and M. J. Sepaniak, *Electrophoresis*, 2008, **29**, 1441-1450.
11. R. Keir, E. Igata, M. Arundell, W. E. Smith, D. Graham, C. McHugh and J. M. Cooper, *Analytical Chemistry*, 2002, **74**, 1503-1508.
12. J. Parisi, S. Liang and L. Yu, *Lab on a Chip*, 2013, **13**, 1501-1508.
13. K. Herman, L. Szabo, L. F. Leopold, V. Chis and N. Leopold, *Analytical and Bioanalytical Chemistry*, 2011, **400**, 815-820.
14. M. R. El-Zahry, A. Genner, I. H. Refaat, H. A. Mohamed and B. Lendl, *Talanta*, 2013, **116**, 972-977.
15. Y. Han, R. Lupitskyy, T. M. Chou, C. M. Stafford, H. Du and S. Sukhishvili, *Analytical Chemistry*, 2011, **83**, 5873-5880.
16. S. Bloxham, O. Eicher-Lorka, R. Jakubënas and G. Niaura, *Chemija*, 2002, **13**, 185-189.
17. M. Moskovits and J. S. Suh, *The Journal of Physical Chemistry*, 1984, **88**, 5526-5530.
18. J. S. Suh and M. Moskovits, *Journal of the American Chemical Society*, 1986, **108**, 4711-4718.
19. E. J. Zeman and G. C. Schatz, *Journal of Physical Chemistry*, 1987, **91**, 634-643.
20. C. H. Munro, W. E. Smith, M. Garner, J. Clarkson and P. C. White, *Langmuir*, 1995, **11**, 3712.
21. K. Setoura, Y. Okada, D. Werner and S. Hashimoto, *ACS Nano*, 2013, **7**, 7874-7885.
22. G. Baffou, J. Polleux, H. Rigneault and S. Monneret, *The Journal of Physical Chemistry C*, 2014, **118**, 4890-4898.
23. A. J. Hallock, P. L. Redmond and L. E. Brus, *Proceedings of the National Academy of Sciences of the United States of America*, 2005, **102**, 1280-1284.
24. B. D. Piorek, L. Seung Joon, J. G. Santiago, M. Moskovits, S. Banerjee and C. D. Meinhart, *Proceedings of the National Academy of Sciences of the United States of America*, 2007, **104**, 18898-18901.
25. L. S. Jung and C. T. Campbell, *The Journal of Physical Chemistry B*, 2000, **104**, 11168-11178.
26. F. Kapteijn, J. A. Moulijn and R. Krishna, *Chemical Engineering Science*, 2000, **55**, 2923-2930.
27. J. E. Kolakowski, J. J. Defrank, S. P. Harvey, L. L. Szafraniec, W. T. Beaudry, K. Lai and J. R. Wild, *Biocatalysis and Biotransformation*, 1997, **15**, 297-312.
28. A. D. Bochevarov, E. Harder, T. F. Hughes, J. R. Greenwood, D. A. Braden, D. M. Philipp, D. Rinaldo, M. D. Halls, J. Zhang and R. A. Friesner, *International Journal of Quantum Chemistry*, 2013, **113**, 2110-2142.
29. J. P. Perdew, K. Burke and M. Ernzerhof, *Physical Review Letters*, 1996, **77**, 3865-3868.
30. R. Ditchfield, W. J. Hehre and J. A. Pople, *The Journal of Chemical Physics*, 1971, **54**, 724-728.
31. M. A. Unger, H.-P. Chou, T. Thorsen, A. Scherer and S. R. Quake, *Science*, 2000, **288**, 113-116.

